Mohamed Zanaty[1]
Instant-Lab
Ecole Polytechnique Fédérale de Lausanne (EPFL),
Neuchâtel 2000, Switzerland
e-mail: mohamed.zanaty@epfl.ch

Simon Henein
Instant-Lab
Ecole Polytechnique Fédérale de Lausanne (EPFL),
Neuchâtel 2000, Switzerland
e-mail: simon.henein@epfl.ch

Experimental Characterization of a T-Shaped Programmable Multistable Mechanism

Programmable multistable mechanisms (PMM) exhibit a modifiable stability behavior in which the number of stable states, stiffness, and reaction force characteristics are controlled via their programming inputs. In this paper, we present experimental characterization for the concept of stability programing introduced in our previous work (Zanaty et al., 2018, "Programmable Multistable Mechanisms: Synthesis and Modeling," ASME J. Mech. Des., 140(4), p. 042301.) A prototype of the T-combined axially loaded double parallelogram mechanisms (DPM) with rectangular hinges is manufactured using electrodischarge machining (EDM). An analytical model based on Euler–Bernoulli equations of the T-mechanism is derived from which the stability behavior is extracted. Numerical simulations and experimental measurements are conducted on programming the mechanism as monostable, bistable, tristable, and quadrastable, and show good agreement with our analytical derivations within 10%. [DOI: 10.1115/1.4040173]

1 Introduction

Multistable mechanisms are mechanical devices with more than one stable state. A stable state is the deformation of the mechanism at which its energy is minimum, implying that a zero force is required for maintaining such state. The stability behavior of a multistable mechanism can be characterized by its strain energy, reaction force, secant, and tangential stiffness and degree of stability (DOS), which represents the number of its stable states, as illustrated in our previous work [1].

Bistable mechanisms are the most common family of multistable mechanisms in which $\mathrm{DOS} = 2$ [2]. Examples of bistable mechanisms include buckled beams [3,4], Young's mechanism [5], slider crank mechanism, and the four bar mechanism [6]. Multistable mechanisms in which $\mathrm{DOS} > 2$ can be constructed by the combination of bistable mechanisms. Serial combination of N-bistable mechanisms can increase DOS to 2^N. Parallel combination of bistable mechanisms can modify DOS as illustrated in the double Young tristable mechanism [7] and the double tensural tristable mechanism [8]. Orthogonal combination of bistable mechanisms can also achieve higher order multistability as demonstrated in Ref. [9]. Multistable mechanisms are beneficial for low power switching applications as medical devices [10], radio frequency systems [11], and micromechanical computations [12] as they require zero force for maintaining their stable states. Furthermore, multistable mechanisms exhibit a wide spectrum behavior due to their fast switching response, which qualifies them as energy harvesting devices [13].

Programmable multistable mechanisms (PMM) are a family of multistable mechanisms whose stability behavior is controlled via external inputs, known as *programing inputs* introduced in Ref. [1]. These inputs modify mechanism DOS, the position of equilibrium states and their stiffness. PMM are characterized by the number of their independent programing inputs, called degree of programming (DOP). For instance, an N-DOP PMM represents a PMM with N independent programming inputs. An example of 1-DOP PMM is the axially loaded beam mechanism [4]. It has one programming input, the axial load of the beam, which programs its DOS to be either one or two. Combination of 1-DOP PMM increases DOS. Serial combination of two 1DOP Miura origami mechanisms leads to a PMM, in which monostability, bistability, and quadrastability can be achieved [14].

In our previous work [1], we demonstrated, both analytically and numerically, that T-combination of two 1-DOP double parallelogram mechanisms (DPM), connected in a way similar to Ref. [15], forms a PMM, which can be programmed as monostable, bistable, tristable, or quadrastable mechanism. Moreover, we found that tuning the programming inputs enables constant force response, whereby zero force monostable, constant force monostable, zero force bistable, constant force bistable, and zero force tristable mechanisms can be achieved. Stability programming enables new applications such as medical devices, mechanical computation, and threshold sensing. We applied PMM to develop retinal vein cannulation needles [16], in which the stiffness of the mechanism is programmed to control the cannulation force. The contributions of this paper are

(1) Experimental validation of the concept of stability programing
(2) Experimental characterization of the stability behavior of the T-mechanism, a generic example of programmable multistable mechanisms discussed in Ref. [1].
(3) Extension of the analytical model in Ref. [1] to parallelogram mechanism having rectangular hinges.

The paper is arranged as follows: First, we briefly review the operation of 2-DOP T-combined DPM. After that, we provide an analytical model of T-combined DPM consisting of rectangular beam hinges. A prototype of the T-mechanism is manufactured using electrodischarge machining (EDM). Then, we discuss the measurement setup and the results, as compared to our analytical and numerical calculations.

2 Programmable T-Shaped Multistable Mechanism

A T-combined DPM consists of two modules orthogonally connected. Each module is an axially loaded DPM with two parallel beams centrally connected by a rigid block, as illustrated in Fig. 1(*a*). Module 1 is fixed on one extremity and axially guided by programming input p_1 on the other extremity. Module 2 is

[1]Corresponding author.
Contributed by the Mechanisms and Robotics Committee of ASME for publication in the Journal of Mechanical Design. Manuscript received January 4, 2018; final manuscript received April 6, 2018; published online June 8, 2018. Assoc. Editor: Massimo Callegari.

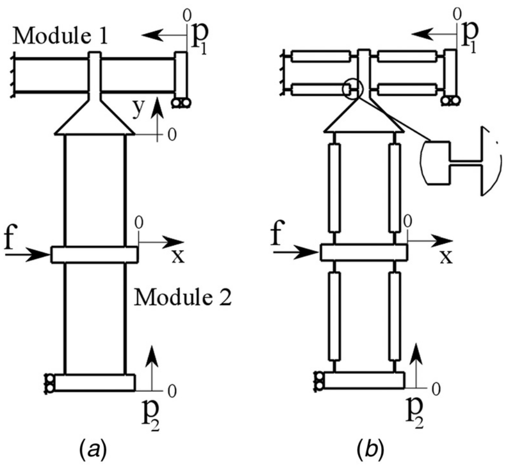

Fig. 1 Two degree of programing T-combined DPM composed of (*a*) distributed stiffness blades and (*b*) lumped stiffness rectangular hinges

Table 1 Degree of stability of the T-mechanism as a function of the programming inputs, p_1, p_2

p_1	p_2	DOS
$p_1 < p_1^{cr}$	$p_2 < p_2^c$	1
$p_1 > p_1^{cr}$	$p_2 < p_2^a$	1
$p_1 < p_1^{cr}$	$p_2 > p_2^c$	2
$p_1 > p_1^{cr}$	$p_2^a < p_2 < p_2^b$	2
$p_1 > p_1^{cr}$	$p_2^b < p_2 < p_2^c$	3
$p_1 > p_1^{cr}$	$p_2 > p_2^c$	4

connected to the central block of module 1 in the lateral direction of the beams of module 1 on one extremity. The other extremity of module 2 is guided by programming input p_2. An actuation input x is applied to the central block of module 2 in the lateral direction of its beams.

The stability behavior of the mechanism depends on the values of p_1 and p_2. We define p_1^{cr} as the minimum value of p_1 at which module 1 buckles with sufficient lateral force to buckle module 2. Similarly, p_2^c is the maximum value of p_2 at which the lateral stiffness of module 2 is zero at $x = 0$.

If $p_1 < p_1^{\text{cr}}$, the mechanism can function either as a monostable or bistable mechanism. If $p_2 > p_2^c$, the mechanism is bistable with unstable state at $x = 0$. If $p_2 < p_2^c$, the mechanism is monostable with a stable state at $x = 0$.

In the case of $p_1 > p_1^{\text{cr}}$, module 1 has three equilibrium states in the lateral direction of its beams at $y = \lambda_2^a, \lambda_2^b, \lambda_2^c$, where $\lambda_2^a < \lambda_2^b < \lambda_2^c$. States at $y = \lambda_2^a, \lambda_2^c$ denote stable states and λ_2^b represents unstable state.

If $p_2 < \lambda_2^a$, the mechanism is monostable as module 1 cannot reach its stable states. If $\lambda_2^a < p_2 < \lambda_2^b$, module 1 can reach one of its stable states but cannot surpass its unstable state and the mechanism is bistable. If $\lambda_2^b < p_2 < p_2^c$, module 1 can surpass its unstable state and behaves as a tristable mechanism. If $p_2 > p_2^c$, the mechanism is quadrastable, where p_2 is sufficient to exhibit negative stiffness at $x = 0$.

We define p_2^a and p_2^b as the values of the programming input, p_2 corresponding to the lateral displacement of module 1, λ_2^a, λ_2^b, respectively, at $x = 0$. Table 1 summarizes the range of the programming inputs for a given DOS. It should be noted that

(1) The values of p_2^a, p_2^b, p_2^c depend on p_1.
(2) The value of p_1^{cr} depends mainly on the dimensions of the mechanism.

The concept of stability programming of T-mechanism is still valid for different geometrical variants of parallelogram mechanisms, in which distributed stiffness blades are replaced by rectangular beam hinges, as given in Fig. 1(*b*).

In this paper, we study T-combined DPM with rectangular beam hinges. They are simpler to manufacture using EDM, compared to distributed stiffness blades discussed in our previous work [1], and have a relatively longer stroke compared to circular notch hinges [17]. In the rest of the paper, we will refer to the T-combined DPM with rectangular hinges as *T-mechanism*, for short.

Figure 2 illustrates a T-mechanism with width w. Module 1 has four beams of length ℓ_1 with rigid links of length r_1 and compliant rectangular hinges of length c_1 and thickness t_1. Module 1 is axially loaded by a spring, referred to as *programming spring*, of stiffness k_r with length ℓ_r and thickness t_r. Module 2 has four beams of length ℓ_2 with rigid links of length r_2 and rectangular hinges of length c_2 and thickness t_2. The thickness of the rigid links is ten times that of the hinges.

We replaced the central rigid block of module 2 by two rigid blocks connected by two hinges, as shown in Fig. 2, to avoid kinematic over constraints, as illustrated by the equivalent rigid body diagram of the mechanism in Fig. 3. This modification does not affect the stability behavior of the mechanism. There are three

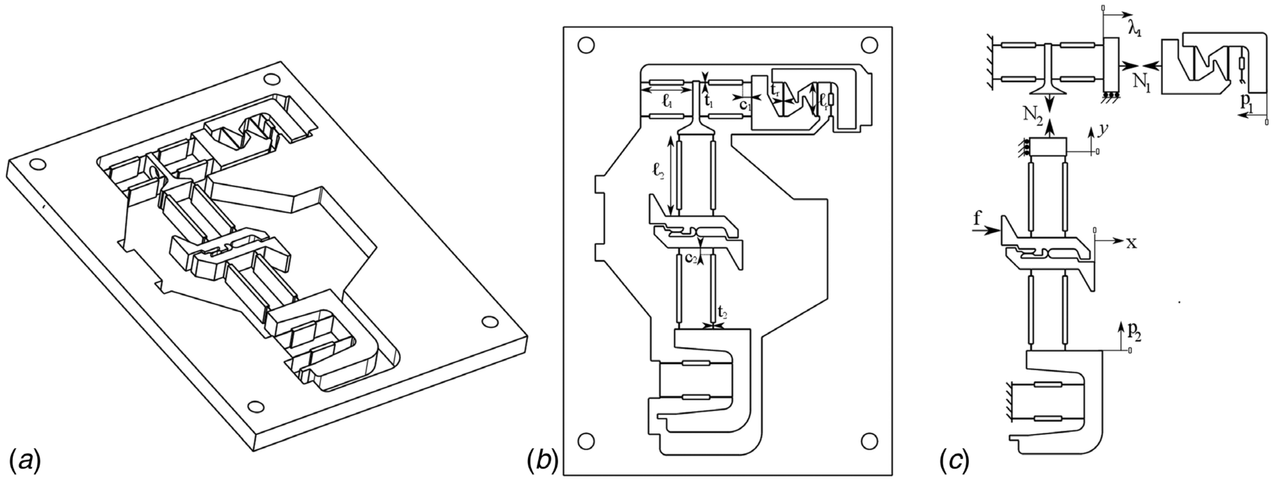

Fig. 2 (*a*) T-mechanism, (*b*) key dimensions, and (*c*) forces and displacements

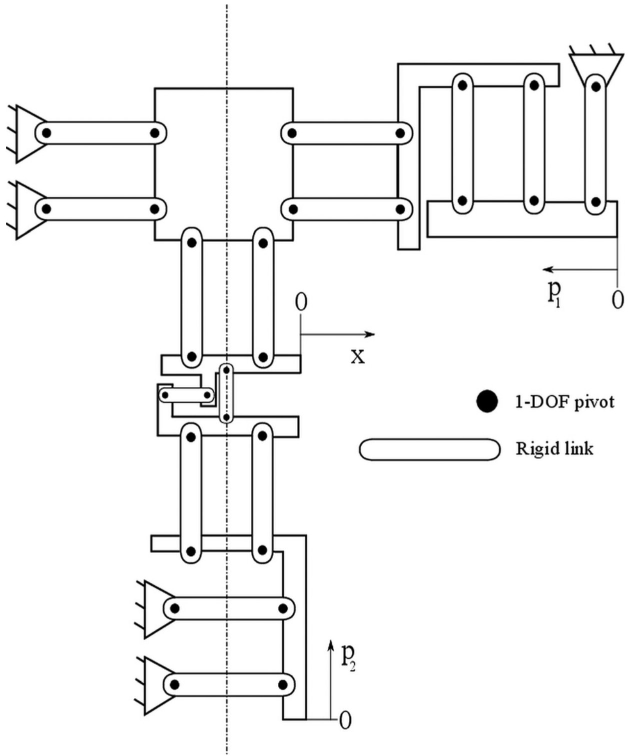

Fig. 3 Equivalent rigid body diagram of the T-mechanism

degrees-of-freedom controlled by programing inputs p_1, p_2, and actuation input x.

As illustrated in our previous paper [1], the stability behavior of the T-mechanism depends on the stiffness ratio of the programming spring to module 1, η_1, stiffness ratio of module 1 to module 2, η_2, and length ratio of the beams of module 2 to module 1, α_2, such that

$$\eta_1 = \frac{I_r \ell_1^3}{I_1 \ell_r^3}, \quad \eta_2 = \frac{I_1 \ell_2^3}{I_2 \ell_1^3}, \quad \alpha_2 = \frac{\ell_2}{\ell_1} \tag{1}$$

We introduce the parameters a_{01}, $a_{02,}$ which denote the ratio of the length of rectangular hinges to the beam length of module 1 and module 2, respectively

$$a_{01} = \frac{c_1}{\ell_1}, \quad a_{02} = \frac{c_2}{\ell_2} \tag{2}$$

3 Analytical Model

We calculate the reaction force f of the mechanism upon applying a displacement x. The reaction force is represented as a seventh-order polynomial from which the stability behavior of the mechanism can be quantified, i.e., DOS, positions of equilibrium states, and their stiffness. Our model is based on the following assumptions:

(1) A linear elastic material is used with Young's modulus Y.
(2) The shear strain of compliant elements is negligible such that Euler–Bernoulli equations can be applied.
(3) Compliant elements are not buckled in their second or higher order buckling modes.
(4) Lateral forces of module 1 and module 2 are negligible compared to the buckling load of the beams of the programming spring.
(5) The displacement range of the beams is within their intermediate range [18].

We normalize all forces of module 2 by $Ywt_2^3/(12\ell_2^2)$ and displacements of module 2 by ℓ_2. Similarly, the forces of module 1 are normalized by $Ywt_1^3/(12\ell_1^2)$ and displacements by ℓ_1.

Following the same procedure discussed in Ref. [1], we derived the reaction force of the T-mechanism having rectangular hinges as a seventh-order polynomial. We first evaluate the relation between displacement x and axial displacements λ_1 and λ_2 of module 1 and module 2, respectively, as illustrated in Fig. 2(*c*). Then, we calculate the axial loads N_1 and N_2 as functions of x. As discussed in Ref. [17], the secant stiffness of module 2 depends on N_2. Based on that, the reaction force of module 2, which represents the reaction force of the mechanism is calculated.

On applying lateral displacement x to the central block of module 2, axial displacement λ_2 occurs [1,18]

$$\lambda_2 = p_2 - \frac{6\Psi_2}{5} x^2 \tag{3}$$

where,

$$\Psi_2 = \frac{15 - 50a_{02} + 60a_{02}^2 - 24a_{02}^3}{2\left(3 - 6a_{02} + 4a_{02}^2\right)^2}$$

ignoring the elastic component of the axial displacement of the compliant beams.

The two modules are orthogonally connected such that the axial displacement of module 2 is equivalent to the lateral displacement of module 1, leading to the following axial displacement of module 1 [1,18]

$$\lambda_1 = -\frac{6\alpha_2^2 \Psi_1}{5} \lambda_2^2 \tag{4}$$

where

$$\Psi_1 = \frac{15 - 50a_{01} + 60a_{01}^2 - 24a_{01}^3}{2\left(3 - 6a_{01} + 4a_{01}^2\right)^2}$$

Substituting Eq. (3) in Eq. (4)

$$\lambda_1 = -\frac{6\alpha_2^2 \Psi_1 p_2^2}{5} + \frac{72\alpha_2^2 \Psi_1 \Psi_2 p_2}{25} x^2 - \frac{216\alpha_2^2 \Psi_1 \Psi_2^2}{125} x^4 \tag{5}$$

Axial displacement λ_1 loads the programing spring imposing an axial load N_1 on module 1 [1,17]

$$N_1 = 24\eta_1 (p_1 + \lambda_1) \tag{6}$$

which modifies the secant lateral stiffness of module 1 such that [1,18]

$$k_s^{p1} = \frac{48}{\Gamma_1} - \frac{12}{5} \Psi_1 N_1 \tag{7}$$

where,

$$\Gamma_1 = \frac{1}{2a_{01}\left(3 - 6a_{01} + 4a_{01}^2\right)}$$

Since module 1 is laterally displaced by λ_2, it imposes an axial load on module 2 [18]

$$N_2 = \eta_2 k_s^{p1} \lambda_2 \tag{8}$$

The lateral reaction force of module 2 is [1,18]

$$f = \left(\frac{48}{\Gamma_2} - \frac{12}{5} \Psi_2 N_2\right) x \tag{9}$$

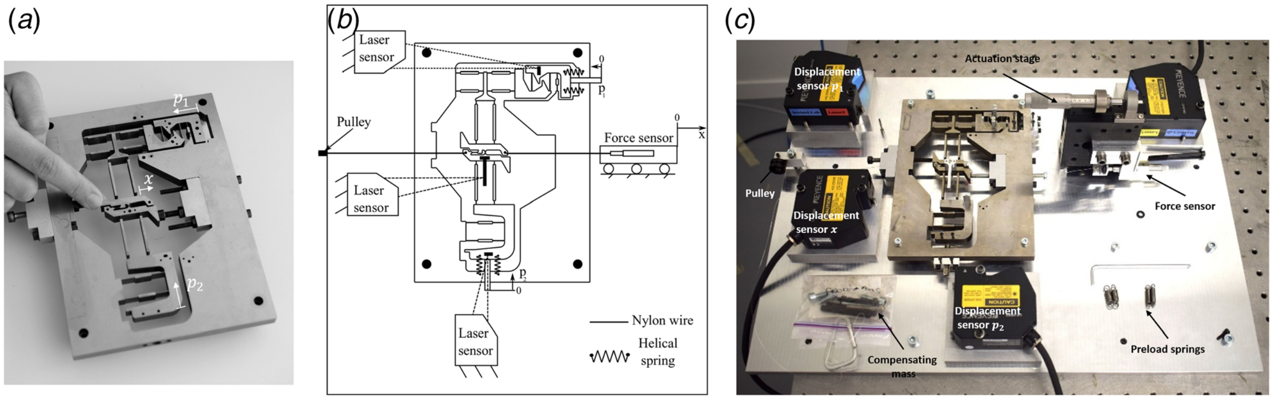

Fig. 4 (*a*) T-mechanism monolithically manufactured by EDM, (*b*) schematic representation of the measurement setup, and (*c*) realization of the measurement setup

where,

$$\Gamma_2 = \frac{1}{2a_{02}\left(3 - 6a_{02} + 4a_{02}^2\right)} \tag{10}$$

Substituting Eqs. (5)–(8) in Eq. (9), the reaction force f of the mechanism can be written as

$$f = x\Phi(x^2) \tag{11}$$

where,

$$\Phi(z) = \beta_0 + \beta_1 z + \beta_2 z^2 + \beta_3 z^3 \tag{12}$$

and,

$$\begin{aligned}
\beta_0 &= \frac{48}{\Gamma_2} - \frac{576\eta_2\Psi_2}{5\Gamma_1}p_2 + \frac{3456\eta_1\eta_2\Psi_1\Psi_2}{25}p_1p_2 \\
&\quad - \frac{20736\eta_1\eta_2\Psi_1^2\Psi_2\alpha_2^2}{125}p_2^3 \\
\beta_1 &= \frac{3456\eta_2\Psi_2^2}{25\Gamma_1} - \frac{20736\eta_1\eta_2\Psi_1\Psi_2^2}{125}p_1 \\
&\quad + \frac{373248\alpha_2^2\eta_1\eta_2\Psi_1^2\Psi_2^2}{625}p_2^2 \\
\beta_2 &= \frac{-2239488\alpha_2^2\eta_1\eta_2\Psi_1^2\Psi_2^3}{3125}p_2 \\
\beta_3 &= \frac{4478976\alpha_2^2\eta_1\eta_2\Psi_1^2\Psi_2^4}{15625}
\end{aligned} \tag{13}$$

The stability behavior of the mechanism can be extracted from the polynomial $\Phi(z)$ [1], where

(1) DOS is estimated by calculating the sign alternation of the coefficients of $\Phi(z)$ and the sign of its discriminant for given p_1, p_2.
(2) Equilibrium positions, q_i, are the square root of the positive-valued zeros of $\Phi(z)$.

$$q_0 = 0, \quad q_i^{\pm} = \pm\sqrt{z_i}, \quad i = 1, 2, 3 \tag{14}$$

(3) The value of the critical buckling load p_1^{cr} is the zero of the discriminant of β_0 where [1]

$$p_1^{\mathrm{cr}} = \frac{5}{6\Gamma_1\eta_1\eta_2} + \frac{126}{127}\left(\frac{\alpha_2^2}{\eta_1^2\eta_2^2\Gamma_2^2\Psi_1\Psi_2^2}\right)^{1/3} \tag{15}$$

(4) The values of p_2^a, p_2^b, and p_2^c are the zeros of the cubic polynomial, β_0, where $p_2^a < p_2^b < p_2^c$ if p_2^a, p_2^b exist.
(5) The tangential stiffness of the mechanism at its equilibrium states, q_i, is the first derivative of the reaction force with respect to the displacement x at equilibrium positions

$$k^t = \left.\frac{\partial f}{\partial x}\right|_{x=q_i} \tag{16}$$

4 Numerical Simulations

We use COMSOL FEM to model the stability behavior of the mechanism and calculate its reaction force and strain energy for different values p_1, p_2. The solid mechanics module is used, including the geometric nonlinearity. The displacement control method is utilized, as it is easier to converge, being a single-valued problem. The actuation displacement x applied at the central block of module 2 is swept and the reaction force is evaluated. The strain energy of the mechanism is estimated by integrating the stored energy density over the volume of the mechanism. Mesh convergence tests are performed to ensure the validity of the solution.

5 Fabrication

The T-mechanism was manufactured out of BOHLER K390 steel [19] using EDM, as shown in Fig. 4(*a*). EDM is used to manufacture reliable compliant elements of maximum length to thickness ratio of 60 [17]. We selected the dimensions of the T-mechanism in Table 2 such that monostability, bistability, tristability, and quadrastability can be experimentally verified based on the dimensional analysis in Ref. [1]. We used Leica M125 stereoscope [20] for dimension measurements with a resolution down

Table 2 Dimensions of the T-mechanism

Dimension	Description	Designed	Measured
w	Beam width	10 (mm)	10 (mm)
	Programing spring		
ℓ_r	Beam length	15 (mm)	15 (mm)
t_r	Beam thickness	350 (μm)	345 (μm)
	Module 1		
ℓ_1	Beam length	23 (mm)	23 (mm)
t_1	Hinge thickness	80 (μm)	78 (μm)
c_1	Hinge length	4.0 (mm)	3.9 (mm)
	Module 2		
ℓ_2	Beam length	36 (mm)	36 (mm)
t_2	Hinge thickness	50 (μm)	49 (μm)
c_2	Hinge length	3 (mm)	2.9 (mm)

to 50 (nm). The inherent tolerance in the EDM technique leads to differences between designed and measured dimensions as given in Table 2.

6 Experimental Setup

We constructed an experimental measurement setup that consists of three displacement Keyence laser sensors, LK-H082 [21], to measure the imposed values of p_1, p_2, and x. Aluminum reflecting blocks are mounted on the mechanism as references planes for the sensors as illustrated in Figs. 4(*b*) and 4(*c*). Displacement sensors used for measuring p_1, p_2 are configured to the range $\pm 2\,(\mathrm{mm})$ with a resolution of $25\,(\mathrm{nm})$. The actuation displacement sensor is configured to measure the range of $\pm 16\,(\mathrm{mm})$ with a resolution of $100\,(\mathrm{nm})$.

We apply manually the programming inputs via micrometric screws, while helical springs are used to apply negative values of the programing inputs. The actuation input is applied via a 1-DOF micrometric stage on which piezo-electric Kistler force sensor, type 9207, is mounted [22]. The sensor is connected to the central block of module 2 via a nylon wire. The force sensor is configured for the range of $\pm 5\,(N)$ with a resolution of $1\,(\mathrm{mN})$. A known mass is used to compensate for the negative reaction force of the mechanism to avoid snapping. The mass is connected to the central block of module 2 via a wire and a pulley. All the sensors are calibrated before the measurement.

We use national instrument cRIO 9035 [23] for the control of the measurement setup and data acquisition. Analog to digital converter NI9220 [24] and charge amplifier Kistler 5171A4 [25] are used for the interface of displacement and force sensors, respectively.

7 Results and Discussion

The dimensional variability of the manufacturing process and the measurements errors are accounted for by using a constant correction factor. This factor is determined by curve fitting the reaction force, as calculated using the analytical model, with experimental measurements when the mechanism is programmed as monostable.

In this section, we use the symbols p_1, p_2, x, and f to denote the explicit values of the programming inputs of module 1, module 2, actuation input, and reaction force, respectively, instead of representing their normalized values. We present and discuss the results according to the different stability regions of the T-mechanism introduced in Ref. [1].

7.1 Monostable Region. The mechanism has only one stable state, i.e., $\mathrm{DOS} = 1$ when $p_1 < p_1^{\mathrm{cr}}$ and $p_2 < p_2^c$ or $p_1 > p_1^{\mathrm{cr}}$ and $p_2 < p_2^a$. Figure 5 gives the stable state of the mechanism, q_0,

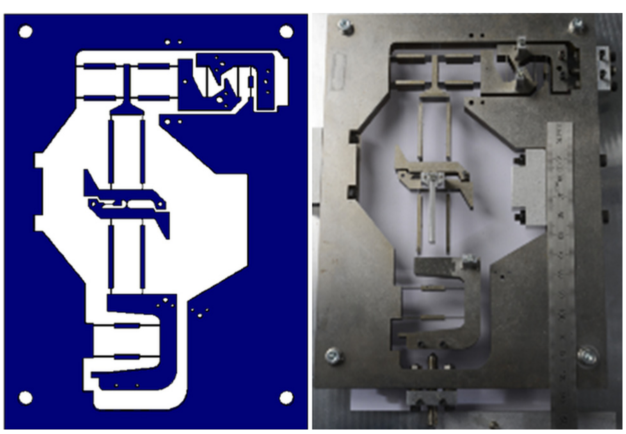

Fig. 5 Stable state q_0 of the mechanism programmed in monostable region based on FEM (left) and experiment (right)

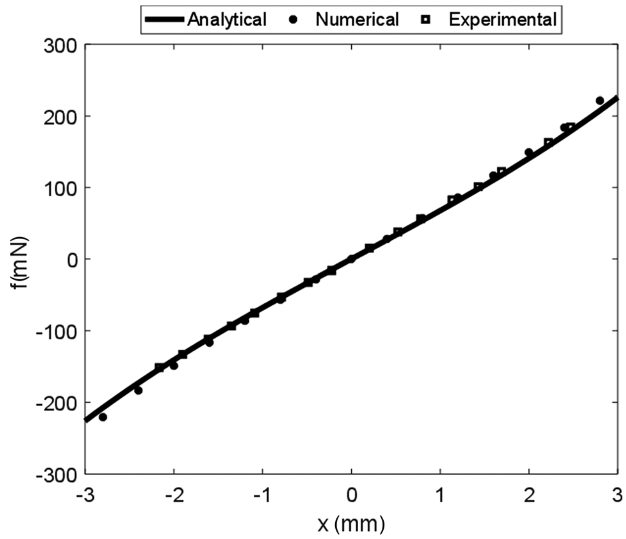

Fig. 6 The reaction force of the mechanism when programmed as monostable for $p_1 = 0.0\,(\mathrm{mm})$ and $p_2 = 0.0\,(\mathrm{mm})$

which occurs at $x = 0$. The reaction force of the mechanism is depicted in Fig. 6 based on the analytical calculations, numerical simulations, and experimental measurements showing a good match.

Upon increasing either p_1 for given p_2 or p_2 for given p_1, the mechanism stiffness at its stable state decreases until it reaches zero at $p_2 = p_2^a$ for $p_1 > p_1^{\mathrm{cr}}$ or $p_2 = p_2^c$ for $p_1 < p_1^{\mathrm{cr}}$.

7.2 Bistable Region. There are two regions in which the mechanism distinctly exhibits bistability.

7.2.1 Region I. This region is defined when $p_1 < p_1^{\mathrm{cr}}$ and $p_2 > p_2^c$, where module 2 buckles. Figure 7 gives the equilibrium states based on numerical simulations and experimental stable states where $q_1^{\pm}$ are the stable states and q_0 is unstable state.

As p_1 increases for a given p_2, the stiffness of the mechanism at its equilibrium position decreases till it reaches zero at $p_2^c = p_2$. However, the stiffness increases by increasing p_2 for a given p_1.

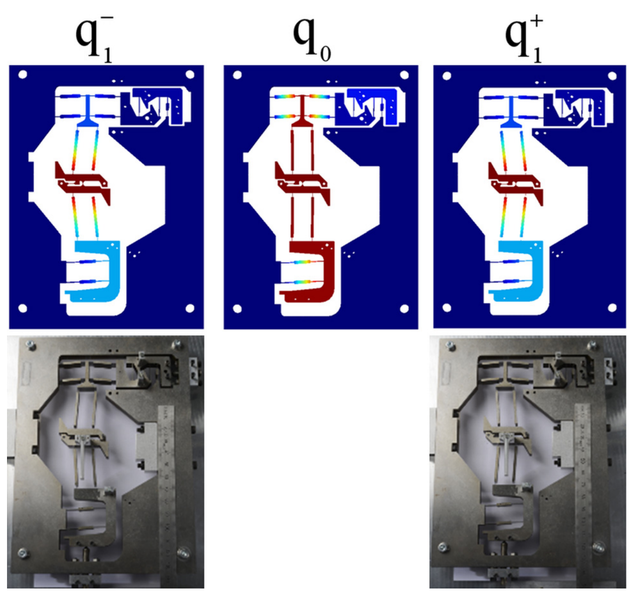

Fig. 7 Stable states, $q_1^{\pm}$ and unstable state, q_0 of the mechanism programmed in bistable region I based on FEM (top) and experiment (bottom)

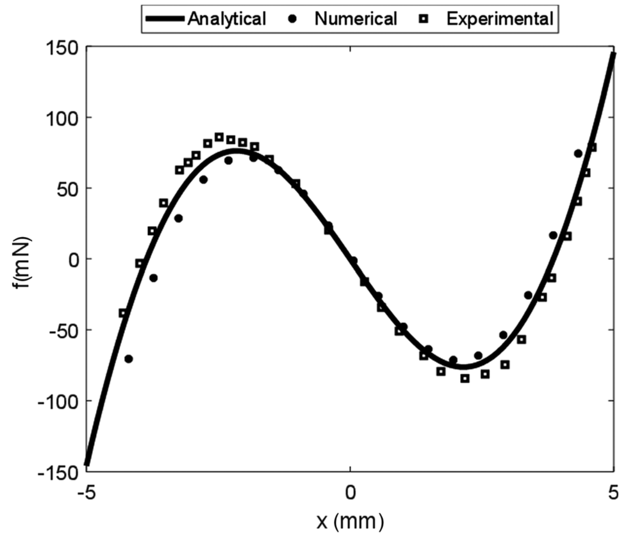

Fig. 8 The reaction force of the mechanism programmed as bistable in region I for $p_1 = -0.15\,(\mathrm{mm})$, $p_2 = 1.1\,(\mathrm{mm})$

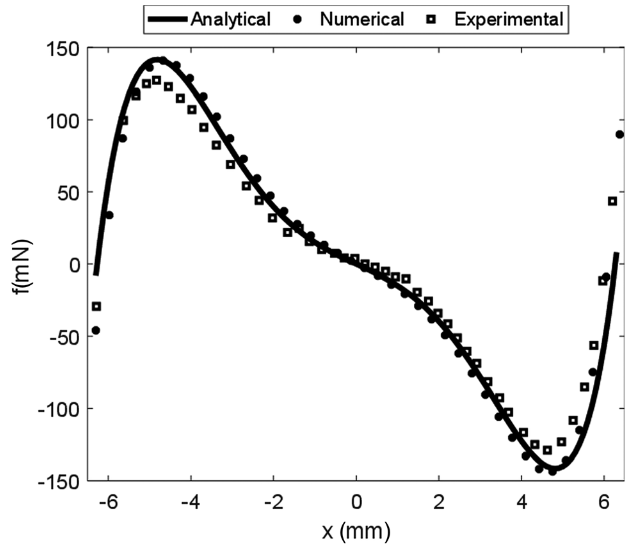

Fig. 10 The reaction force of the mechanism programmed as bistable in region II for $p_1 = 0.39\,(\mathrm{mm})$, $p_2 = -0.9\,(\mathrm{mm})$

Figure 8 illustrates the reaction force of the T-mechanism at $p_1 = -0.15\,(\mathrm{mm})$, $p_2 = 1.1\,(\mathrm{mm})$.

7.2.2 Region II. This region is defined by $p_1 > p_1^{\mathrm{cr}}$ and $p_2^a < p_2 < p_2^b$. The mechanism has unstable state q_0 at $x = 0$. Figure 9 illustrates the equilibrium states of the mechanism based on numerical simulations and the equivalent experimental stable states, where $q_3^{\pm}$ are stable and q_0 is unstable. Figure 10 shows the reaction force of the mechanism for $p_1 = 0.39\,(\mathrm{mm})$ and $p_2 = -0.9\,(\mathrm{mm})$.

The mechanism exhibits lower stiffness magnitude around its unstable state, compared to its stable states. As p_2 increases for a given p_1, the stiffness of the mechanism increases around its stable states $q_3^{\pm}$; however, the stiffness magnitude around q_0 may increase or decrease, depending on the range of the applied p_2. In the case of p_1 increase for a given p_2, the stiffness magnitude for both stable states $q_3^{\pm}$ and unstable state q_0 increases.

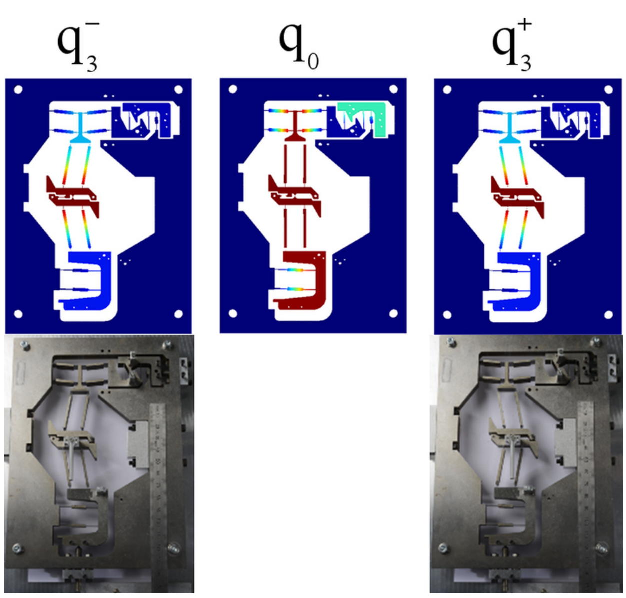

Fig. 9 Stable states, $q_3^{\pm}$ and unstable state, q_0 of the mechanism programmed in bistable region II based on FEM (top) and experiment (bottom)

7.3 Tristable Region. The mechanism exhibits tristability when $p_1 > p_1^{\mathrm{cr}}$ and $p_2^b < p_2 < p_2^c$. Figure 11 gives the equilibrium states of the mechanism based on numerical simulations and their equivalent experimental stable states where q_0, $q_3^{\pm}$ are stable and $q_2^{\pm}$ are unstable. The reaction force of the mechanism for $p_1 = 0.36\,(\mathrm{mm})$, $p_2 = 2.8\,(\mathrm{mm})$ for imposed displacement x is given in Fig. 12.

As p_1 increases for a given p_2, the stiffness of equilibrium states, q_0, $q_2^{\pm}$, $q_3^{\pm}$, increases. On increasing p_2 for a given p_1, the stiffness magnitude of stable states $q_3^{\pm}$ and unstable states $q_2^{\pm}$ increases while the stiffness of the stable state q_0 may increase or decrease depending on p_2.

7.4 Quadrastable Region. The mechanism exhibits quadrastability when $p_1 > p_1^{\mathrm{cr}}$ and $p_2 > p_2^c$. Figure 13 illustrates the seven equilibrium states of the mechanism, based on numerical simulations and the equivalent experimental stable states where q_0 and $q_2^{\pm}$ are unstable and $q_1^{\pm}$ and $q_3^{\pm}$ are stable.

Figure 14 illustrates the reaction force of the mechanism for $p_1 = 0.36\,(\mathrm{mm})$, $p_2 = 0.8\,(\mathrm{mm})$. As p_1 increases for a given p_2, the stiffness of states $q_2^{\pm}$, $q_3^{\pm}$ increases and the stiffness of states q_0, $q_1^{\pm}$ decreases. On increasing p_2 for a given p_1, the stiffness magnitude of all equilibrium states, q_0, $q_1^{\pm}$, $q_2^{\pm}$, $q_3^{\pm}$ increases. It is clear that the switching force between q_1^+ and q_1^- is far lower than the switching force from q_1^+ to q_3^+. This is an intrinsic limitation of the T-mechanism.

7.5 Summary. The reaction force of the T-mechanism in the different stability regions was measured. A discrepancy of less than 10% is found in estimating the switching forces for certain values of programming inputs between the analytical model on one side and experimental results and numerical simulations on the other. This is attributed to neglecting higher order nonlinear stiffness terms in the model, as in the case when the mechanism displacement exceeds the intermediate displacement range. We also ignore the axial parasitic displacement of the central block of module 1 on calculating the axial force of module 2, which affects the mechanism overall stiffness. Moreover, the effect of the elastic component of the axial displacement of the beams is ignored. The friction of the pulley, which was not considered in the model, is likely to affect the measured stiffness. However, we find the model sufficient for first order estimation of the stability behavior of the T-mechanism.

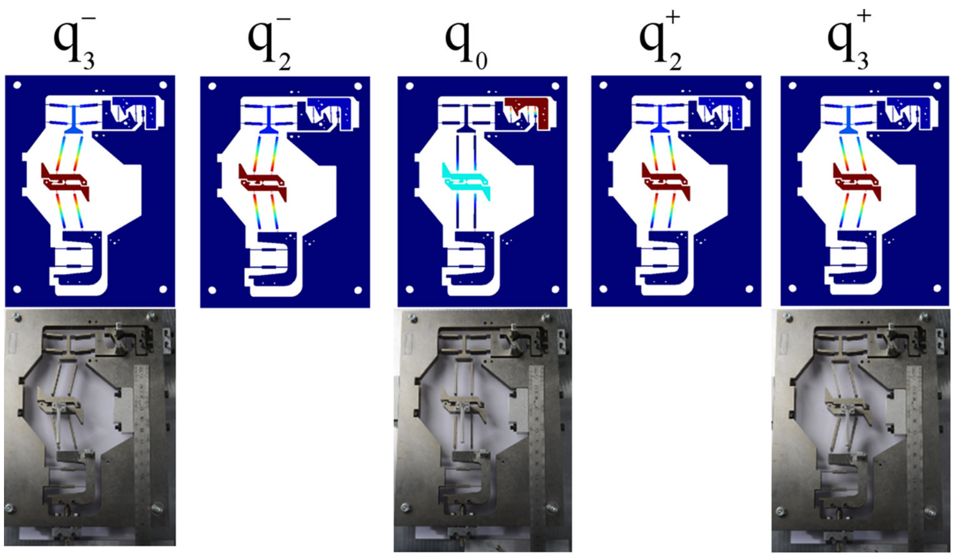

Fig. 11 Stable states, q_0, $q_3^{\pm}$ and unstable states, $q_2^{\pm}$ of the mechanism programmed in tristable region based on FEM (top) and experiment (bottom)

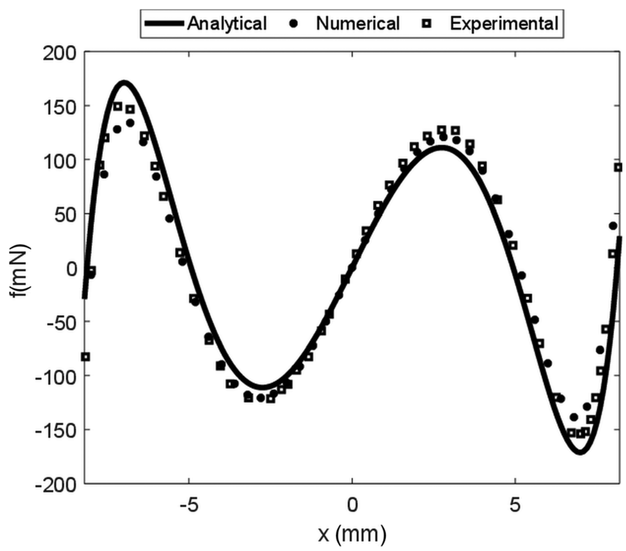

Fig. 12 The reaction force of the mechanism programmed as tristable for $p_1 = 0.37$ (mm), $p_2 = 0.0$ (mm)

The effect of the programming inputs on the stiffness magnitude of the T-mechanism, at its equilibrium states based on Eq. (16), is summarized in Table 3, where $\uparrow$ indicates an increase, $\downarrow$ indicates a decrease, $\rightarrow$ indicates no change, and $\uparrow\downarrow$ denotes dependency of the trend on the range of the applied programming inputs.

7.6 Programming Diagram. The programming diagram gives the number of stable states of the T-mechanism, i.e., DOS, upon changing its programming inputs p_1, p_2.

The DOS can be found by evaluating the sign of the discriminant of Φ and the number of sign alteration between the coefficients β_0, β_1, β_2, β_3 in Eq. (13) [1]. The values of stability boundaries p_1^{cr}, p_2^a, p_2^b, p_2^c were measured experimentally as reported in Fig. 15 and show good match with analytical computations within less than 7%.

7.7 Equilibrium Positions. We study the effect of the programming inputs p_1, p_2 on the positions of equilibrium states, which are the square roots of the positive-valued zeros of $\Phi(z)$, as given in Eq. (14). We fix one of the programming inputs and sweep the other one.

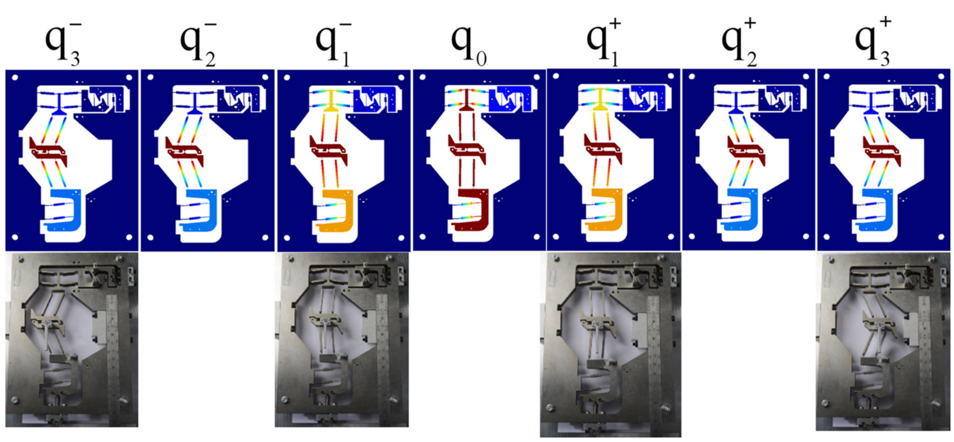

Fig. 13 Stable states, $q_1^{\pm}$, $q_3^{\pm}$, and unstable states, q_0, $q_2^{\pm}$ of the mechanism programmed in quadrastable region based on FEM (top) and experiment (bottom)

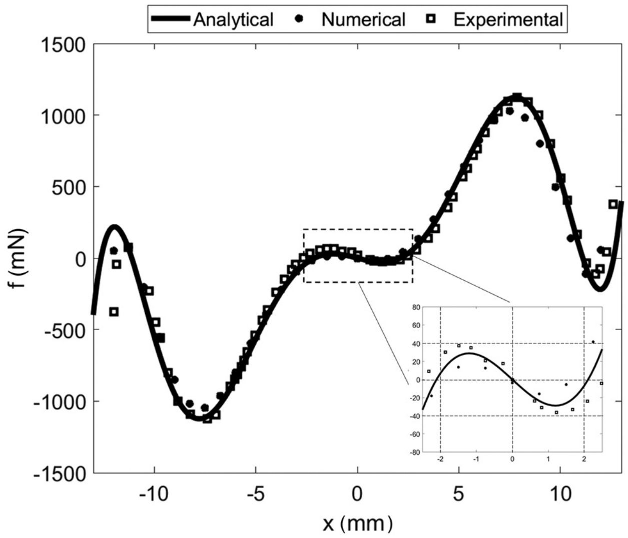

Fig. 14 The reaction force of the mechanism programmed as quadrastable for $p_1 = 0.36$ (mm), $p_2 = 2.8$ (mm). The inset illustrates the reaction force upon switching between second and third stable states.

Table 3 Effect of the programming inputs on stiffness magnitude of the existing equilibrium states

		Programming inputs		Stiffness at equilibrium states			
Region	DOS	p_1	p_2	q_0	$q_1^{\pm}$	$q_2^{\pm}$	$q_3^{\pm}$
Monostable	1	↑	→	↓			
		→	↑	↓			
Bistable I	2	↑	→	↓	↓		
		→	↑	↑	↑		
Bistable II	2	↑	→	↑			↑
		→	↑	↑↓			↑
Tristable	3	↑	→	↑		↑	↑
		→	↑	↑↓		↑	↑
Quadrastable	4	↑	→	↓	↓	↑	↑
		→	↑	↑	↑	↑	↑

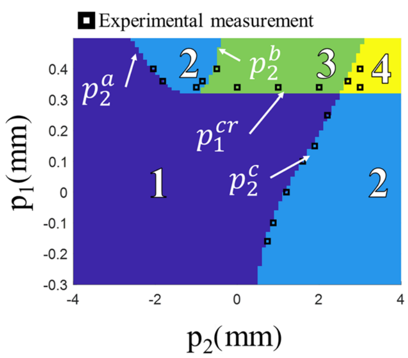

Fig. 15 Programming diagram of the T-mechanism in which stability boundaries p_1^{cr}, p_2^a, p_2^b, p_2^c are experimentally verified

7.7.1 Fixing p_1 and Sweeping p_2. There are two qualitatively different equilibrium diagrams as illustrated by the selected values in Fig. 16(*a*).

The first case occurs when $p_1 < p_1^{cr}$, the mechanism is monostable with a stable state q_0 at $x = 0$. At $p_2 = p_2^c$, the stable state q_0 becomes unstable and bifurcates into two stable states $q_1^{\pm}$ as given in Fig. 16(*b*). The value of the bifurcation node $p_2 = p_2^c$ depends on p_1. As p_1 increases, p_2^c increases as well.

The second case occurs when $p_1 > p_1^{cr}$ as illustrated in Fig. 16(*c*). In this case, the mechanism is monostable for $p_2 < p_2^a$ with a stable state q_0 at $x = 0$. At $p_2 = p_2^a$, the stable state becomes unstable and bifurcates into two stable states $q_3^{\pm}$. The mechanism becomes bistable upon increasing p_2. At $p_2 = p_2^b$, the unstable state q_0 becomes stable and bifurcates into two unstable states $q_2^{\pm}$. The mechanism is tristable with increasing p_2. At $p_2 = p_2^c$, q_0 bifurcates again into two stable states, $q_1^{\pm}$ and becomes unstable. The mechanism is quadrastable for $p_2 > p_2^c$.

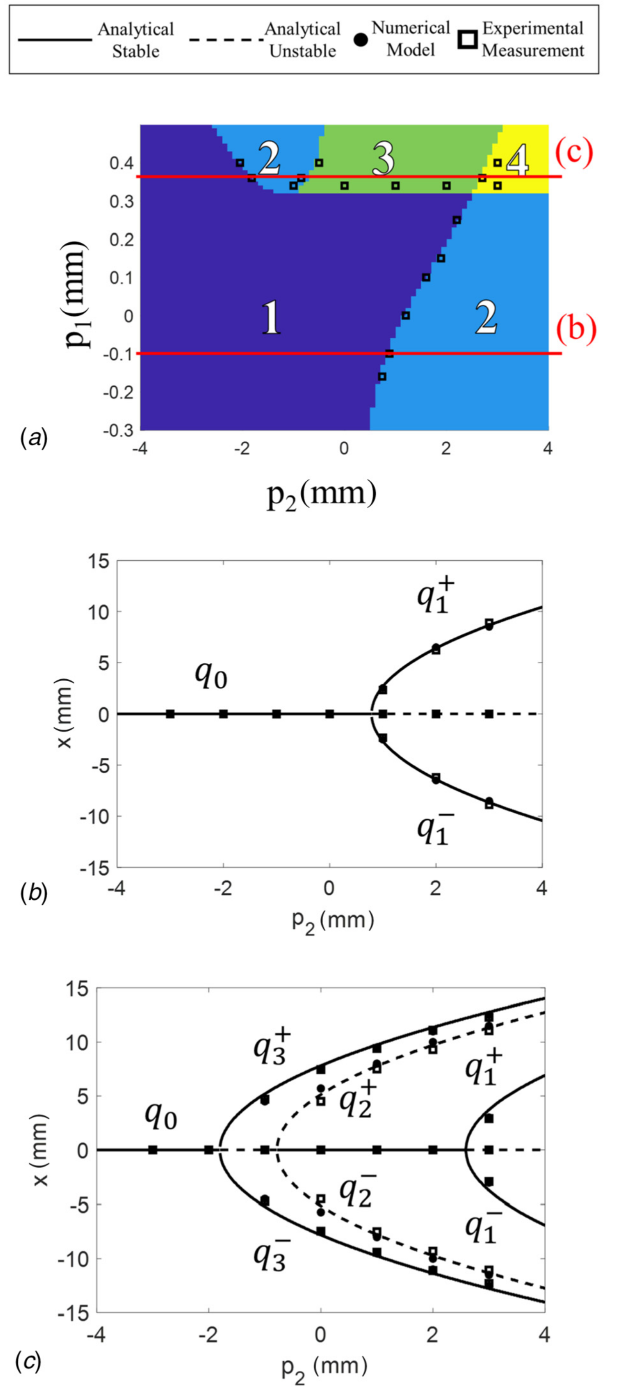

Fig. 16 (*a*) Selected p_1 values of the calculated equilibrium position diagrams as p_2 varies from −4 (mm) to 4 (mm), equilibrium positions diagram at (*b*) $p_1 = -0.1$ (mm), and (*c*) $p_1 = 0.35$ (mm) verified both numerically and experimentally

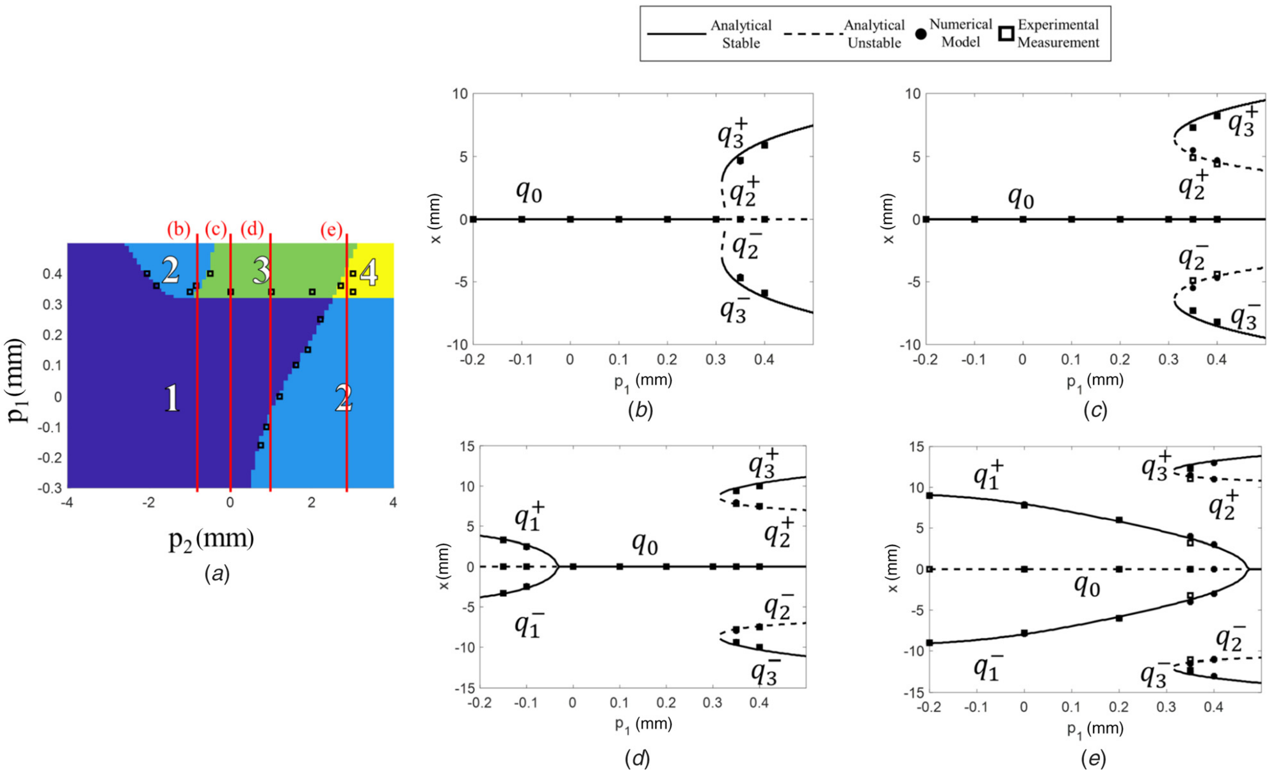

Fig. 17 (*a*) Selected p_2 values of the calculated equilibrium position diagrams as p_1 varies from −0.2 (mm) to 0.5 (mm). Equilibrium positions diagram at (*b*) $p_2 = -1$ (mm), (*c*) $p_2 = 0$ (mm), (*d*) $p_2 = 1$ (mm), and (*e*) $p_2 = 3$ (mm) verified numerically and experimentally.

7.7.2 Fixing p_2 and Sweeping p_1. When p_2 is fixed as p_1 increases, the value p_2^a decreases and p_2^b, p_2^c increase. Both the values p_2^a, p_2^b exist only for $p_1 \geq p_1^{\mathrm{cr}}$. We consider different cases illustrated in Fig. 17(*a*).

If $p_2^a > p_2$ for all values of p_1, the mechanism is monostable with a stable state q_0 at $x = 0$. In the case that p_2 is selected such that $p_2^a < p_2$ and $p_2^b > p_2$ for a certain range of p_1, the mechanism shows both monostability and bistability. At $p_2^a = p_2$, pitch-fork bifurcation occurs at which stable state q_0 becomes unstable and bifurcates into two stable states $q_3^{\pm}$ [1].

If p_2 is selected such that $p_2^b < p_2$ and $p_2^c > p_2$ for a given range of $p_1 > p_1^{\mathrm{cr}}$, the mechanism can show monostability, tristability, and bistability, as illustrated in Fig. 17(*b*). For $p_1 < p_1^{\mathrm{cr}}$, the mechanism has a stable state q_0 at $x = 0$. At $p_1 = p_1^{\mathrm{cr}}$, saddle-node bifurcation occurs and stable states, $q_3^{\pm}$, unstable states, $q_2^{\pm}$ emerge. The mechanism is tristable.

As p_1 increases, p_2^b increases as well. When $p_2^b = p_2$, inverted pitchfork bifurcation occurs. The stable state q_0 becomes unstable and the two unstable states, $q_2^{\pm}$ merge at $x = 0$ and the mechanism becomes bistable.

On increasing p_2 and sweeping p_1, the value of the bifurcation node $p_2^b = p_2$ increases and the equilibrium states, $q_2^{\pm}$, $q_3^{\pm}$ move apart from $x = 0$. When $p_2^b < p_2$ and $p_2^c > p_2$ over the entire range of p_1, the mechanism functions as monostable for $p_1 < p_1^{\mathrm{cr}}$ and tristable mechanism for $p_1 > p_1^{\mathrm{cr}}$, as illustrated in Fig. 17(*c*).

If p_2 is selected such that $p_2^c < p_2$ for a given range of $p_1 < p_1^{\mathrm{cr}}$ and $p_2^b < p_2$, $p_2^c > p_2$ for $p_1 > p_1^{\mathrm{cr}}$, the mechanism can exhibit bistability, monostability and tristability upon changing p_1, as illustrated in Fig. 17(*d*). For $p_2^c < p_2$, the mechanism has two stable states, $q_1^{\pm}$ and unstable state q_0. As p_1 increases, p_2^c increases. At $p_2^c = p_2$, the stable state q_0 becomes stable and the two stable states $q_1^{\pm}$ merge at $x = 0$ and the mechanism is monostable. At $p_1 = p_1^{\mathrm{cr}}$, saddle-node bifurcation occurs and stable states, $q_3^{\pm}$ and unstable states, $q_2^{\pm}$ emerge rendering the mechanism tristable.

On further increase of p_2, the value of the bifurcation node p_2^c increases. If $p_2^c = p_2$ at $p_1 > p_1^{\mathrm{cr}}$, the mechanism shows quadrastability for $p_2^c < p_2$ and tristability for $p_2^c > p_2$ while $p_1 > p_1^{\mathrm{cr}}$ as illustrated in Fig. 17(*e*).

8 Conclusion

In this paper, we experimentally verified the concept of stability programming using T-combined double parallelogram mechanism consisting of rectangular beam hinges. An analytical model of the mechanism was also derived. The reaction force is represented as a seventh order polynomial from which the stability behavior of the mechanism is extracted.

Reaction force, programming diagram and bifurcation diagrams of equilibrium positions were calculated analytically, numerically and experimentally where a mismatch of less than 10% was found.

References

[1] Zanaty, M., Vardi, I., and Henein, S., 2018, "Programmable Multistable Mechanisms: Synthesis and Modeling," ASME J. Mech. Des., **140**(4), p. 042301.
[2] Howell, L. L., Magleby, S. P., and Olsen, B. M., 2013, *Handbook of Compliant Mechanisms*, Wiley, Hoboken, NJ.
[3] Qiu, J., Lang, J. H., and Slocum, A. H., 2004, "A Curved-Beam Bistable Mechanism," Microelectromech. Syst., J., **13**(2), pp. 137–146.
[4] Cazottes, P., Fernandes, A., Pouget, J., and Hafez, M., 2009, "Bistable Buckled Beam: Modeling of Actuating Force and Experimental Validations," ASME J. Mech. Des., **131**(10), p. 101001.
[5] Jensen, B. D., Howell, L. L., and Salmon, L. G., 1998, "Introduction of Two-Link In-Plane, Bistable Compliant MEMS," ASME Paper No. DETC98/MECH-5837.
[6] Jensen, B. D., and Howell, L. L., 2003, "Identification of Compliant Pseudo-Rigid-Body Four-Link Mechanism Configurations Resulting in Bistable Behavior," ASME J. Mech. Des., **125**(4), pp. 701–708.

[7] Chen, G., and Du, Y., 2013, "Double-Young Tristable Mechanisms," ASME J. Mech. Rob., **5**(1), p. 011007.
[8] Chen, G., Wilcox, D. L., and Howell, L. L., 2009, "Fully Compliant Double Tensural Tristable Micromechanisms (DTTM)," J. Micromech. Microeng., **19**(2), p. 025011.
[9] Chen, G., Gou, Y., and Zhang, A., 2011, "Synthesis of Compliant Multistable Mechanisms Through Use of a Single Bistable Mechanism," ASME J. Mech. Des., **133**(8), p. 081007.
[10] Receveur, R. A., Marxer, C. R., Woering, R., Larik, V. C., and de Rooij, N.-F., 2005, "Laterally Moving Bistable MEMS DC Switch for Biomedical Applications," J. Microelectromech. Syst., **14**(5), pp. 1089–1098.
[11] Oberhammer, J., Tang, M., Liu, A.-Q., and Stemme, G., 2006, "Mechanically Tri-Stable, True Single-Pole-Double-Throw (SPDT) Switches," J. Micromech. Microeng., **16**(11), p. 2251.
[12] Merkle, R. C., 1993, "Two Types of Mechanical Reversible Logic," Nanotechnology, **4**(2), p. 114.
[13] Harne, R., and Wang, K., 2013, "A Review of the Recent Research on Vibration Energy Harvesting Via Bistable Systems," Smart Mater. Struct., **22**(2), p. 023001.
[14] Fang, H., Li, S., Ji, H., and Wang, K., 2017, "Dynamics of a Bistable Miura-Origami Structure," Phys. Rev. E, **95**(5), p. 052211.
[15] Chen, G., Aten, Q. T., Zirbel, S., Jensen, B. D., and Howell, L. L., 2010, "A Tristable Mechanism Configuration Employing Orthogonal Compliant Mechanisms," ASME J. Mech. Rob., **2**(1), p. 014501.
[16] Zanaty, M., 2018, "Programmable Multistable Mechanisms," Ph.D. thesis, Ecole Polytechnique Federale De Lausanne, Lausanne, Switzerland.
[17] Henein, S., ed., 2017, *The Art of Flexure Mechanism Design*, EPFL Press, Lausanne, Switzerland.
[18] Awtar, S., Slocum, A. H., and Sevincer, E., 2007, "Characteristics of Beam-Based Flexure Modules," ASME J. Mech. Des., **129**(6), pp. 625–639.
[19] Voestalpine, 2017, "BÖHLER K390 MICROCLEAN," Voestalpine, Linz, Austria, accessed Dec. 17, 2017, www.bohler-edelstahl.com/en/K390PM.php
[20] Leica Microsystems, 2017, "Encoded Stereo Microscopes Leica M125 C, M165 C, M205 C, M205 A," Leica Microsystems, Wetzlar, Germany, accessed Dec. 17, 2017, https://www.leica-microsystems.com/products/stereo-microscopes-macroscopes/research/details/product/leica-m125-c/
[21] Keyence, 2017, "Measurement Sensors," Keyence, Osaka, Japan, accessed Dec. 17, 2017, www.keyence.com/products/measure/laser-1/lk-g5000/models/lk-h082/index.jsp
[22] Kistler, 2017, "1-Component Low Force Sensor, Fz up to $\pm$50 N / $\pm$11.24 lbf," Kistler, Winterthur, Switzerland, accessed Dec. 17, 2017, http://www.ni.com/pdf/manuals/376935c_02.pdf
[23] NI, 2017, "NI cRIO 9035," National Instruments, Austin, TX, accessed Dec. 17, 2017, http://www.ni.com/pdf/manuals/376935c_02.pdf
[24] NI, 2017, "NI-9220," National Instruments, Austin, TX, accessed Dec. 17, 2017, http://www.ni.com/documentation/en/c-series-voltage-input-module/latest/9220/specs/
[25] Kistler, 2017, "Kistler's 5171A Charge Amplifier Module," Kistler, Winterthur, Switzerland, accessed Dec. 17, 2017, https://www.kistler.com/en/products/components/signal-conditioning/charge-amplifier-module-ki-5171a-for-ni-compactrio/